T2R2 東京科学大学 リサーチリポジトリ
Science Tokyo Research Repository

論文 / 著書情報
Article / Book Information

Title	Mid-infrared photothermoelectric detector using topological insulator BiSb thin film
Authors	Hajime Nishiyama, Pham Nam Hai, Yukio Kawano
Citation	Optical Materials Express, Vol. 16, Issue 3, pp. 603-610
Pub. date	2026, 2
Copyright	(c) 2026 Optica Publishing Group. Users may use, reuse, and build upon the article, or use the article for text or data mining, so long as such uses are for non-commercial purposes and appropriate attribution is maintained. All other rights are reserved.
DOI	http://dx.doi.org/10.1364/OME.571598

Powered by T2R2 (Science Tokyo Research Repository)

Research Article Vol. 16, No. 3 / 1 Mar 2026 / Optical Materials Express 603
Optical Materials EXPRESS

Mid-infrared photothermoelectric detector using topological insulator BiSb thin film

HAJIME NISHIYAMA,[1,2,*] PHAM NAM HAI,[1] AND YUKIO KAWANO[2,3,4]

[1]Department of Electrical and Electronic Engineering, Institute of Science Tokyo, Tokyo 152-8550, Japan
[2]Department of Electrical, Electronic, and Communication Engineering, Chuo University, Tokyo 112-8551, Japan
[3]National Institute of Informatics, Tokyo 101-8430, Japan
[4]Kanagawa Institute of Industrial Science and Technology, Kanagawa 243-0435, Japan
*nishiyama.h.ab@m.titech.ac.jp

Abstract: We demonstrate a mid-infrared (MIR) photothermoelectric (PTE) detector based on a $Bi_{90}Sb_{10}$ thin film, a topological insulator with strong MIR absorption and a high Seebeck coefficient. BiSb films were deposited by magnetron sputtering, a scalable and cost-effective method, on both sapphire and flexible Kapton substrates. The PTE response was systematically evaluated for various device geometries. A maximum voltage of 27 μV was obtained for a 16 mm × 0.25 mm × 80 nm film on sapphire. A 3 × 3 array of 4 mm × 0.25 mm elements was demonstrated. Finally, we demonstrated a large PTE response of 170 μV with improved detectivity D^* of $1.1 \cdot 10^5$ cm$\sqrt{\text{Hz}}$/W for a BiSb-based PTE device on a Kapton flexible substrate. These results highlight the potential of sputtered BiSb thin films for large-area MIR detector arrays with low fabrication cost.

© 2026 Optica Publishing Group under the terms of the Optica Open Access Publishing Agreement

1. Introduction

The mid-infrared (MIR) region of electromagnetic spectrum is important for characterizing the vibrational modes of various chemical and biomolecular compounds. As a result, this spectral region is highly suitable for chemical or biological sensing, with many applications in various fields, such as medical diagnostics, infrastructure monitoring, and security scanning [1]. There are mainly two types of infrared detector; quantum detector and thermal detector [2]. Quantum detector converts light directly into electrical signal, while thermal detector converts light into heat and then heat into resistance (bolometer), pressure (Golay cell), and so on. Each type of detectors has advantages and disadvantages. Quantum detector operates at high speed and high sensitivity, however requires cooling setup. For an infrared quantum detectors' material, a narrow bandgap semiconductor such as HgCdTe is a good candidate [3,4]. However, HgCdTe is known to take cost and time to grow an epitaxial thin film of this material using the molecular beam epitaxy (MBE) method. Also, there is a restriction of substrate material on which a film of HgCdTe semiconductor can be grown epitaxially. On the other hand, thermal detector operates at room temperature but at low speed and low sensitivity. Thermal detector has a potential to be a useful infrared detector operating at room temperature, if speed and sensitivity are improved. One method of infrared thermal detector is photothermoelectric (PTE) effect [5], which involves a conversion of light into heat, and heat into electrical signal. The former conversion can be realized with absorbing material in infrared region. The latter conversion can be achieved by the thermoelectric Seebeck effect. Seebeck effect is a phenomenon that a voltage is generated along a temperature difference of a material, and it is expressed as $V = S\Delta T$, where V is a voltage, S is Seebeck coefficient, ΔT is a temperature difference. Recently, PTE detector has been demonstrated using carbon nanotube (CNT) [6]. Furthermore, a camera with an array of CNT-based PTE detectors deposited on a flexible substrate has been demonstrated [6], which showcases the potential of this technology. However, CNT-based PTE detectors require

#571598 https://doi.org/10.1364/OME.571598
Journal © 2026 Received 25 Jun 2025; revised 23 Sep 2025; accepted 12 Oct 2025; published 17 Feb 2026

Optical Materials EXPRESS

solution-based processes [7], which may limit the spatial resolution and the size of the substrate. As another candidate material, we have recently found that the narrow gap topological insulator BiSb has high absorption in the MIR region (Figure S1) [8]. Also, BiSb has relatively large Seebeck coefficient [9,10,11]. Furthermore, high-quality BiSb can be deposited not only by the MBE technique but also by the magnetron sputtering technique, which can significantly reduce fabrication costs and increase the substrate size [12]. Therefore, BiSb has a potential to be a good material for PTE MIR detection material with low fabrication costs and large substrate size. This is especially important when the substrate is required to be large and flexible, such as large non-intrusive cargo scanner, which can have size of ~ 1 m or larger.

In this work, we measured PTE voltage of a $Bi_{90}Sb_{10}$ film under MIR laser irradiation. We first prepared $Bi_{90}Sb_{10}$ film with size of $l \times w \times t$ (l: length = 4 mm, 10 mm,16 mm, w: width = 0.25 mm, 0.5 mm, 2 mm, t: thickness =80 nm) by magnetron sputtering and lift-off process on rigid sapphire substrates, and conducted PTE measurement with MIR laser and digital multimeter. The results show that PTE voltage increases with decreasing width and increasing length of the film. The sample of 16 mm × 0.25 mm × 80 nm reached the maximum voltage about 27 μV and the noise floor of 1 μV. Based on the results, a 3 × 3 array of 4 mm × 0.25 mm elements was fabricated, assuming a spatial resolution of 5 mm × 5 mm. The elements show reasonable response around 7-10 μV, indicating that BiSb can be used as a large area detector. Finally, we fabricated a BiSb PTE detector (4 mm × 0.5 mm × 81 nm) on a flexible Kapton (poly-oxydiphenylene-pyromellitimide) substrate, and demonstrated a large voltage of ~ 170 μV. Our results show that BiSb can be used as a flexible MIR detector with high signal-to-noise ratio for large area detector arrays with low fabrication cost.

2. Methods

We prepared samples as shown in figure S2. We prepared ribbon-shaped $Bi_{90}Sb_{10}$ thin films of $l \times w \times t$ (l: length = 4 mm, 10 mm,16 mm, w: width = 0.25 mm, 0.5 mm, 2 mm, t: thickness =80 nm) by magnetron sputtering and lift-off technique on sapphire substrates. Pt/Ta film was then formed onto the edge of the BiSb film as electrodes. For fabrication of $Bi_{90}Sb_{10}$ thin film on a flexible Kapton substrate, we first attached the Kapton substrate to a rigid substrate, and then use it for optical lithography, BiSb deposition, and lift-off. After that, the Kapton substrate with BiSb PTE detector was peeled off from the rigid substrate for PTE measurement. We measured the thickness of the $Bi_{90}Sb_{10}$ film by using X-ray reflection (XRR) spectroscopy. For PTE measurements, we used a quantum cascade laser with the wavelength of 4.33 μm and the power of 28.6 mW (L12004-2310H-E, Hamamatsu Photonics) to irradiate the samples with a 1.5 mm spot size. The PTE voltage was measured by a digital multimeter (34980A, KEYSIGHT) and recorded by 5 times a second. In addition, we evaluated the rise time of PTE voltage to reach 80% of the maximum from the light-on time and the fall time of the PTE voltage to reach 20% from the light-off time, respectively. The measurement setup is shown in figure S3.

3. Results and discussion

Figure 1 shows an illustration of a $Bi_{90}Sb_{10}$ PTE detector on a sapphire substrate. The Pt/Ta electrodes were formed to overlap the $Bi_{90}Sb_{10}$ film with an area of 50 μm × w (w: width of $Bi_{90}Sb_{10}$ film). The electrodes were designed long enough to facilitate wire bonding. MIR was irradiated onto the edge of each $Bi_{90}Sb_{10}$ film. The spot position of MIR was adjusted with a laser viewing card.

Figure 2(a)–2(c) show the PTE response of $Bi_{90}Sb_{10}$ slabs on sapphire with a length of 4 mm, 10 mm, and 16 mm, respectively. At each length, we fabricated three types of devices with the width w = 2 mm, 0.5 mm, and 0.25 mm. Figure 2(d) summarizes the PTE maximum voltages of those devices. We observed the general trend that the PTE voltage is higher for longer l and shorter w.

Optical Materials EXPRESS

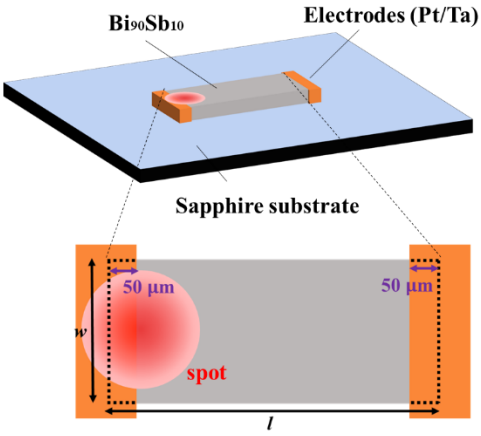

Fig. 1. An illustration of a sample of $Bi_{90}Sb_{10}$ film on a sapphire substrate. Pt/Ta electrodes were formed to overlap the $Bi_{90}Sb_{10}$ film with an area of 50 μm × w.

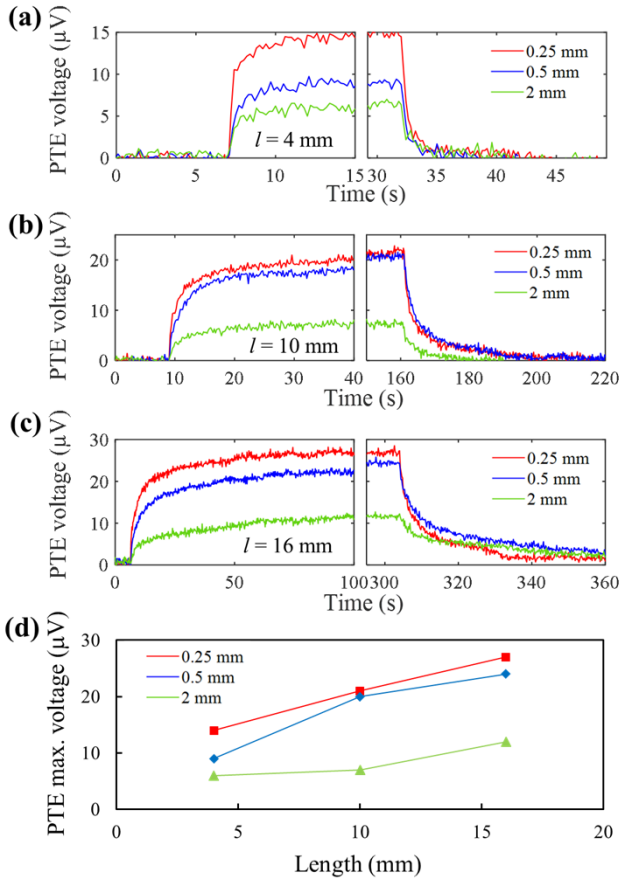

Fig. 2. PTE response of $Bi_{90}Sb_{10}$ films on a sapphire substrate with a length of (a) 4 mm, (b) 10 mm, (c) 16 mm and different widths. (d) PTE maximum voltages of those samples.

Optical Materials EXPRESS

For $l = 4$ mm samples, the maximum voltage is about 14 μV, 9 μV, and 6 μV, for $w = 0.25$ mm, 0.5 mm, and 2 mm, respectively. For $l = 10$ mm samples, the maximum voltage is about 21 μV, 20 μV and 7 μV, for $w = 0.25$ mm, 0.5 mm, 2 mm, respectively. For $l = 16$ mm samples, the maximum voltage is about 27 μV, 24 μV and 12 μV, for $w = 0.25$ mm, 0.5 mm, 2 mm, respectively. These experimental results can be explained qualitatively by the Fourier's law for heat conduction in a $Bi_{90}Sb_{10}$ slab with the length L,

$$q = -k\frac{\Delta T}{L},$$

where q is the heat flux density, k is the thermal conductivity of $Bi_{90}Sb_{10}$, and ΔT is the temperature difference between the two ends of the BiSb slab. At a fixed width, q is a constant, thus ΔT and consequently the maximum PTE voltage increase with longer L. Meanwhile, at a fixed length, q depends on the area-averaged laser power density received by the edge. When the width is 2 mm, which is larger than the laser spot size of about 1.5 mm, the area-averaged laser power density received by the edge is lower because the laser beam is Gaussian. When the width is reduced to 0.5 mm, the area-averaged laser power density received by the edge now approaches the Gaussian center power density, and it reaches maximum when the width is 0.25 mm.

From the data in Figs. 2(a)–2(c), we evaluated the rise time t_{on} and the fall time t_{off} of the PTE voltage. Table 1 shows t_{on} and t_{off} for each sample. We found that PTE response becomes faster with decreasing the size. However, not all the data follows the trend. In this measurement, as the differences between the spot size and the widths are small, it is thought to be in the margin of error, for $l = 4$ mm, 10 mm. For $l = 16$ mm, it takes more time to reach the max voltage and the trend is clearer that the sample of the smallest width is the fastest to reach the max volage. However, we note that there is a trend that, among the samples of a same length, a sample of the smallest width is the fastest to reach a certain voltage. For example, for $l = 4$ mm sample, the fastest to reach 5 μV is $w = 0.25$ mm sample, the slowest is $w = 2$ mm sample, and this is true for $l = 10$ mm, 16 mm samples, too.

Table 1. On-time and off-time of each sample in Fig. 2.

w \ l	4 mm	10 mm	16 mm
0.25 mm	t_{on}~1.4 s, t_{off}~0.2 s	t_{on}~6.2 s, t_{off}~7.8 s	t_{on}~10 s, t_{off}~13 s
0.5 mm	t_{on}~1.3 s, t_{off}~1.2 s	t_{on}~8.0 s, t_{off}~10 s	t_{on}~25 s, t_{off}~32 s
2 mm	t_{on}~1.3 s, t_{off}~1.4 s	t_{on}~6.2 s, t_{off}~5.0 s	t_{on}~30 s, t_{off}~39 s

t_{on}: time to reach 80% of the maximum voltage after light-on.
t_{off}: time to fall to 20% of the maximum voltage after light-off.

Overall, we found that the noise floor is about 1 μV. As this noise is independent of the width and the length of the $Bi_{90}Sb_{10}$ slabs, this can be attributed to the measurement system with many electrical wiring bonding. Further lowering of measurement noise can be possible by using a dedicated measuring circuitry.

We estimated the noise (V_{noise}), noise equivalent power (NEP), and detectivity (D*) of the detectors. As the PTE detector operates under zero voltage and the effect of the flicker noise can be avoided, the thermal noise (Johnson noise) is dominant [5]. The thermal noise (V_{noise}) and the responsivity ($\boldsymbol{R}$) were calculated as follows

$$V_{noise} = \sqrt{4k_B TR}$$

$$\boldsymbol{R} = \frac{V}{P_{effect}},$$

Optical Materials EXPRESS

where k_B is the Boltzmann constant, T is the temperature, R is the resistance, V is the PTE voltage, and P_{effect} is the effective power of irradiated IR at the detector. NEP [13] and D^* [14] were calculated as follows

$$\mathrm{NEP} = \frac{V_{noise}}{\boldsymbol{R}} = \frac{\sqrt{4k_B TR}}{V} P_{effect}$$

$$D^* = \frac{\sqrt{A_{eff}}}{\mathrm{NEP}},$$

where A_{eff} is the area of the detection. The detectivity D^* and NEP are different in that D^* considers A_{eff} while NEP does not. As the laser was Gaussian beam, we calculated A_{eff}, P_{eff} as shown in Fig. 3. These two parameters were calculated by the equation in Fig. 3(b) (numerical calculation by MATLAB).

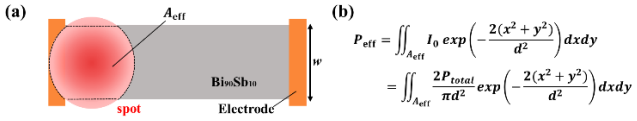

Fig. 3. (a) Illustration of how to calculate P_{eff} for NEP, assuming that the effective area A_{eff} is the region of the Gaussian beam spot that overlaps with the film the area (Gaussian intensity distribution). P_{total} : total power of the laser (=28.6 mW), d : radius of the beam spot (=0.75 mm). (b) The equation to calculate P_{eff}.

The calculations were performed under the condition of $T = 300$ K. The results are shown in Table 2. V_{noise} are ~nV/$\sqrt{\text{Hz}}$, NEP are ~μW/$\sqrt{\text{Hz}}$, and D^* are ~10^4 cm$\sqrt{\text{Hz}}$/W. V_{noise} are 10^3 lower than the noise floor(~1 μV), which further verifies the aforementioned discussion of the cause of the noise floor. Comparing the D^* with that of the recently reported IR PTE detector of Graphene/PEDOT (operating wavelength = 4.3 μm) [15], it is one order lower (6.95 ·10^5 cm$\sqrt{\text{Hz}}$/W).

Table 2. V_{noise}, P_{eff}, NEP and D^* calculated under an assumption as shown in Fig. 3.

	V_{noise}	P_{eff}	NEP	D^*
4 mm × 0.25 mm	7.7 nV/$\sqrt{\text{Hz}}$	7.5 mW	4.1 μW/$\sqrt{\text{Hz}}$	1.5 · 10^4 cm$\sqrt{\text{Hz}}$/W
4 mm × 0.5 mm	5.5 nV/$\sqrt{\text{Hz}}$	14 mW	8.5 μW/$\sqrt{\text{Hz}}$	1.0 · 10^4 cm$\sqrt{\text{Hz}}$/W
4 mm × 2 mm	3.1 nV/$\sqrt{\text{Hz}}$	29 mW	15 μW/$\sqrt{\text{Hz}}$	9.0 · 10^3 cm$\sqrt{\text{Hz}}$/W

Based on these results, we fabricated a 3 × 3 array of 4 mm × 0.25 mm elements, for a cell size of 5 mm × 5 mm. Figure 4(a) shows an illustration of the array. We labelled each row by "A, B, C" and each column by "1,2,3." One edge of three elements in a row (e.g., A1, A2, A3) was connected to a common ground pad for simplification of the measurement setup. Figures 4(b)–4(d) shows the PTE response of the elements. Here, each element was illuminated individually to measure its standalone performance. The timing of laser irradiation was manually aligned across the measurements, as in Fig. 2. The maximum voltages are around 7-10 μV, which are smaller than that of 14 μV observed for the single device with same size in Fig. 2. One possible explanation for the reduction of PTE voltages in the array is that the extra common ground pads around the elements may add extra heat sinks to the large sapphire heat sink, resulting in more heat diffusion away from the edges. This leads to a smaller heat flow in the element and thus smaller PTE response.

From the data in Figs. 4(b)–4(d), we evaluated the rise time t_{on} and the fall time t_{off} of the PTE voltage. Table 3 shows t_{on} and t_{off} for each element. There can be seen a rough trend that

Optical Materials EXPRESS

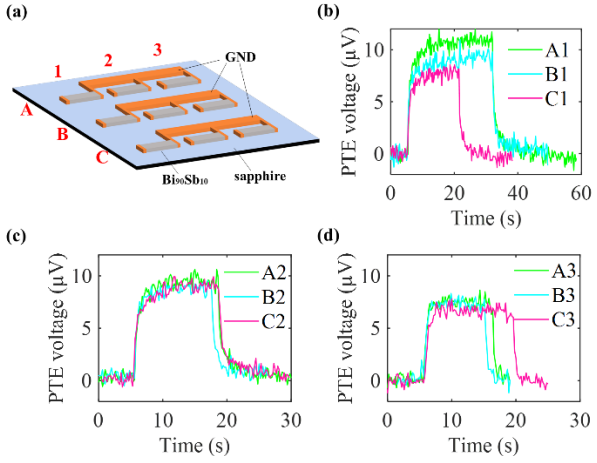

Fig. 4. BiSb PTE array with 3 × 3 elements. (a) An illustration of the array. (b)-(d) PTE responses of each three elements in the same column.

elements with longer ground pads operate slower. For example, the element Al operates slower than the element A3. This can be attributed to the size of the heat sink in the same way as the voltage.

Table 3. On-time and off-time of each sample in Fig. 3.

column / row	1	2	3
A	t_{on}~1.5 s, t_{off}~1.6 s	t_{on}~1.2 s, t_{off}~1.5 s	t_{on}~0.8 s, t_{off}~1.0 s
B	t_{on}~1.5 s, t_{off}~1.2 s	t_{on}~0.7 s, t_{off}~1.2 s	t_{on}~0. 7 s, t_{off}~0.6 s
C	t_{on}~1.4 s, t_{off}~1.0 s	t_{on}~1.7 s, t_{off}~1.7 s	t_{on}~0.7 s, t_{off}~0.9 s

t_{on}: time to reach 80% of the maximum voltage after light-on.
t_{off}: time to fall to 20% of the maximum voltage after light-off.

Despite the smaller PTE voltages, the array can be used as an array detector for MIR imaging when the D^* is good enough.

To further increase the D^*, we fabricated a $Bi_{90}Sb_{10}$ PTE detector (4 mm × 0.5 mm × 81 nm) on a Kapton substrate. The Kapton substrate [16] has a significant lower thermal conductivity than the sapphire substrate [17]. The lower thermal conductivity of Kapton helps reduce the heat diffusion away from the edge and increase the heat flux in the BiSb slab, and leads to higher ΔT and PTE response. Figure 5(a) shows the illustration of a sample. We applied Ag paste to both ends of the slab as electrodes. Figure 5(b) shows the PTE response of the detector, which shows a significantly higher maximum voltage of 170 μV, lower NEP of 0.81μW/$\sqrt{\text{Hz}}$, and higher D^* of $1.1{\cdot}10^5$ cm$\sqrt{\text{Hz}}$/W. The D^* improved by one order and became the same order as that of the IR PTE detector of Graphene/PEDOT ($6.95 \cdot 10^5$ cm$\sqrt{\text{Hz}}$/W) [15]. The response times were t_{on}~ 1 s and t_{off}~1.2s, which are almost the same as that of BiSb/sapphire sample. The response time (thermal time constant) can be evaluated as follows [14]:

$$\tau = \frac{C_T}{G_T},$$

where C_T is the total thermal capacitance (JK^{-1}), G_T is the total thermal conductance (WK^{-1}), of the detector. Representative values of thermal capacity are 0.77 $Jg^{-1}K^{-1}$(sapphire [18]),

Optical Materials EXPRESS

1.09 $Jg^{-1}K^{-1}$(Kapton [19]), and those of thermal conductivity are 30 $Wm^{-1}K^{-1}$(sapphire [17]), 0.20 $Wm^{-1}K^{-1}$(Kapton [19]), respectively. The ratios of thermal capacity/thermal conductivity are 0.026(sapphire), 5.45 (Kapton), respectively. From this calculation, it is estimated that BiSb/Kapton detector operates slower than BiSb/Sapphire detector. The mismatch between this calculated ratio and the actual ratio(~1) can be attributed to the conditions such as the contacts between BiSb and substrate(sapphire, Kapton), the difference of electrodes(Pt/Ta and Ag paste).

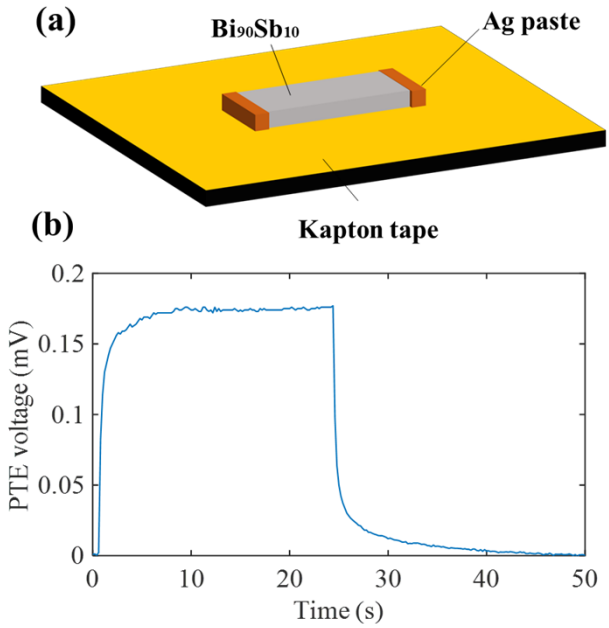

Fig. 5. $Bi_{90}Sb_{10}$ PTE detector on a flexible Kapton substrate. (a) An illustration of a $Bi_{90}Sb_{10}$ slab with a size of 4 mm × 0.5 mm on a Kapton substrate. (b) PTE response of the detector.

The large D^* of our BiSb PTE detector on the Kapton substrate and the recent development of organic semiconductor-based amplifier circuitries [20] indicate that BiSb can be used for a flexible MIR detector with large area and low fabrication costs.

4. Conclusions

We have demonstrated that $Bi_{90}Sb_{10}$ thin films fabricated by magnetron sputtering exhibit strong photothermoelectric responses in the MIR region. The device performance was optimized by adjusting length and width, which followed the thermal transport behavior. A 3 × 3 detector array confirmed that BiSb devices can function as individual elements within an array configuration, suggesting practical applicability for imaging systems. The use of sputtering enables fabrication on large-area and flexible substrates with lower cost and higher throughput compared to epitaxial growth methods. The key advantage lies in BiSb's suitability for scalable array-type MIR detectors using standard thin-film processing techniques. Finally, we note that BiSb is a topological insulator with a giant spin Hall effect [21,22,23], thus new MIR detector concept utilizing the photothermal and spin Seebeck effects [24] is possible in BiSb / ferromagnetic bilayers.

Funding. JST-Mirai Program (JPMJMI23G1); Japan Society for the Promotion of Science (JP23H00169, JP24K01288, JP25H02154, JP25K01289).

Acknowledgements. The XRR measurements were performed at the Materials Analysis Division, Open Facility Center of Institute of Science Tokyo. This work was supported by the Mirai Program (JPMJMI23G1) from the Japan

Optical Materials EXPRESS

Science and Technology Agency, JSPS KAKENHI (JP23H00169, 24K01288, 25H02154, 25K01289) from the Japan Society for the Promotion of Science, and the Innovative Industrial Multi-Scale Sensor Project from the Kanagawa Institute of Industrial Science and Technology.

Disclosures. The authors declare no conflicts of interest.

Data availability. The data that support this work are available from the first author upon reasonable request.

Supplemental document. See Supplement 1 for supporting content.

References

1. A. Rogalski, "Infrared detectors: an overview," Infrared Phys. Technol. **43**(3-5), 187–210 (2002).
2. A. Rogalski, "HgCdTe infrared detector material: history, status and outlook," Rep. Prog. Phys. **68**(10), 2267–2336 (2005).
3. A. Rogalski, "History of infrared detectors," Opto-Electron. Rev. **20**(3), 279–308 (2012).
4. M. Yang, H. Zhou, and J. Wang, "Topological insulators photodetectors; Preparation, advances and application challenges," Mater. Today Commun. **33**, 104190 (2022).
5. D. Suzuki, S. Oda, and Y. Kawano, "A flexible and wearable terahertz scanner," Nat. Photonics **10**(12), 809–813 (2016).
6. L. Takai, Y. Kinoshita, N. Takahashi, *et al.*, "n-type carbon nanotube inks for high-yield printing of ultrabroadband soft photo-imager thin sheets," FlexMat **2**(1), 115–125 (2025).
7. M. Yamamoto, D. Sakai, Y. Matsuzaki, *et al.*, "Mechanically alignable and all-dispenser-printable device design platform for carbon nanotube-based soft-deformable photo-thermoelectric broadband imager sheets," npj Flex Electron. **9**(1), 42 (2025).
8. H. Nishiyama, P. N. Hai, T. Amemiya, *et al.*, "Infrared optical constants n, κ of topological insulator BiSb thin film determined by reflectance-transmittance technique," submitted for publication.
9. F. Völklein and E. Kessler, "Thermoelectric properties of Bi1−xSbx films with $0 < x \leqslant 0.3$," Thin Solid Films **155**(2), 197–208 (1987).
10. T. Teramoto, T. Komine, S. Yamamoto, *et al.*, "Influence of the band structure of BiSb alloy on the magneto-Seebeck coefficient," J. Appl. Phys. **104**(5), 053714 (2008).
11. Y. Ueda, N. H. D. Khang, K. Yao, *et al.*, "Epitaxial growth and characterization of Bi1-xSbx spin Hall thin films on GaAs(111) substrates," Appl. Phys. Lett. **110**(6), 062401 (2017).
12. T. Fan, M. Tobah, T. Shirokura, *et al.*, "Crystal growth and characterization of topological insulator BiSb thin films by sputtering deposition on sapphire substrates," Jpn. J. Appl. Phys. **59**(6), 063001 (2020).
13. D. Suzuki, Y. Ochiai, and Y. Kawano, "Thermal Device Design for a Carbon Nanotube Terahertz Camera," ACS Omega **3**(3), 3540–3547 (2018).
14. A. Das, M. L. Mah, J. Hunt, *et al.*, "Thermodynamically limited uncooled infrared detector using an ultra-low mass perforated subwavelength absorber," Optica **10**(8), 1018–1028 (2023).
15. G. Lu, J. Wang, W. Gao, *et al.*, "Flexible Free-Standing Infrared Photothermoelectric Detector Based on Graphene/PEDOT," IEEE Nanotechnology Mag. **19**(4), 6–13 (2025).
16. D. J. Benford, T. J. Powers, and S. H. Moseley, "Thermal conductivity of Kapton tape," Cryogenics **39**(1), 93–95 (1999).
17. D. Vaca, M. Barry, L. Yates, *et al.*, "Measurements and numerical calculations of thermal conductivity to evaluate the quality of β-gallium oxide thin films grown on sapphire and silicon carbide by molecular beam epitaxy," Appl. Phys. Lett. **121**(4), 042107 (2022).
18. S. Picard, D. T. Burns, and P. Roger, "Measurement of the Specific Heat Capacity of Synthetic Sapphire (α-Al_2O_3) from 293 K to 301 K," Bureau International des Poids et Mesures (2008).
19. DuPont(corp), "DuPont™ Kapton®," https://www.dupont.com/content/dam/electronics/amer/us/en/electronics/public/documents/en/EI-10142_Kapton-Summary-of-Properties.pdf."
20. R. Kawabata, K. Li, T. Araki, *et al.*, "Ultraflexible Wireless Imager Integrated with Organic Circuits for Broadband Infrared Thermal Analysis," Adv. Mater. **36**(15), 309864 (2024).
21. P. N. Hai, "Spin Hall Effect in Topological Insulators," J. Magn. Soc. Jpn. **44**(6), 137–144 (2020).
22. N. H. D. Khang, Y. Ueda, and P. N. Hai, "A conductive topological insulator with large spin Hall effect for ultralow power spin–orbit torque switching," Nat. Mater. **17**(9), 808–813 (2018).
23. T. Fan, N. H. D. Khang, S. Nakano, *et al.*, "Ultrahigh efficient spin orbit torque magnetization switching in fully sputtered topological insulator and ferromagnet multilayers," Sci. Rep. **12**(1), 2998 (2022).
24. K. Uchida, S. Takahashi, K. Harii, *et al.*, "Observation of the spin Seebeck effect," Nature **455**(7214), 778–781 (2008).